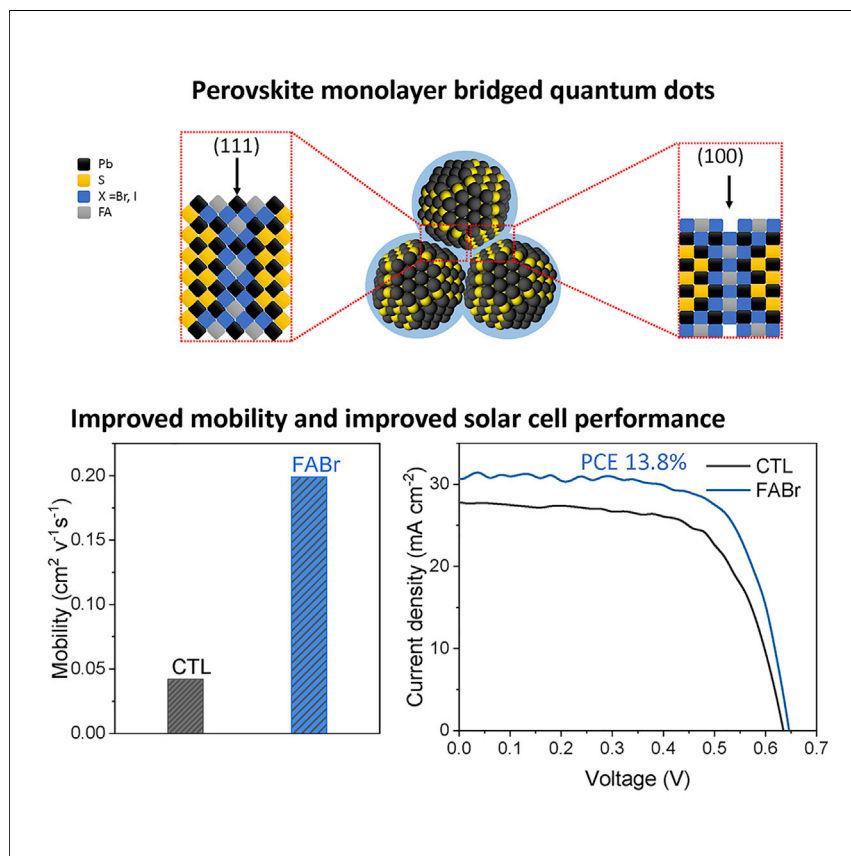


Article

Monolayer Perovskite Bridges Enable Strong Quantum Dot Coupling for Efficient Solar Cells



We report the growth of a monolayer of perovskite that bridges neighboring QDs. This increases interdot coupling, minimizing the distance over which carriers are required to tunnel, all the while maintaining excellent surface passivation. The QD solids provide fully a 3-fold improvement in mobility relative to the best prior well-passivated QD solids, enabling a power conversion efficiency (PCE) of 13.8%, a record among PbS QD solar cells.

Bin Sun, Andrew Johnston, Chao Xu, ..., Oleksandr Voznyy, F. Pelayo García de Arquer, Edward H. Sargent

ted.sargent@utoronto.ca

HIGHLIGHTS

Monolayer of perovskite bridging neighboring quantum dots

A 3-fold improvement in mobility and 2-fold increased diffusion length

A 13.8% PCE, a record among PbS quantum dot solar cells

Article

Monolayer Perovskite Bridges Enable Strong Quantum Dot Coupling for Efficient Solar Cells

Bin Sun,¹ Andrew Johnston,¹ Chao Xu,² Mingyang Wei,¹ Ziru Huang,¹ Zhang Jiang,³ Hua Zhou,³ Yajun Gao,^{4,5} Yitong Dong,¹ Olivier Ouellette,¹ Xiaopeng Zheng,⁴ Jiakai Liu,⁴ Min-Jae Choi,¹ Yuan Gao,¹ Se-Woong Baek,¹ Frédéric Laquai,^{4,5} Osman M. Bakr,⁴ Dayan Ban,² Oleksandr Voznyy,¹ F. Pelayo García de Arquer,¹ and Edward H. Sargent^{1,6,*}

SUMMARY

Solution-processed colloidal quantum dots (CQDs) are promising optoelectronic materials; however, CQD solids have, to date, exhibited either excellent transport properties but fusion among CQDs or limited transport when QDs are strongly passivated. Here, we report the growth of monolayer perovskite bridges among quantum dots and show that this enables the union of surface passivation with improved charge transport. We grow the perovskite layer after forming the CQD solid rather than introducing perovskite precursors into the quantum dot solution: the monolayer of perovskite increases interdot coupling and decreases the distance over which carriers must tunnel. As a result, we double the diffusion length relative to reference CQD solids and report solar cells that achieve a stabilized power conversion efficiency (PCE) of 13.8%, a record among Pb chalcogenide CQD solar cells.

INTRODUCTION

Colloidal quantum dots (CQDs) have attracted interest in solar cell applications due to their tunable band gap and solution processability.^{1–6} CQD device power conversion efficiencies (PCEs) have been increased via improved surface ligand exchanges,^{7,8} increased CQD homogeneity and coupling,⁹ and new device architectures.^{10–14}

To date, the best performance CQD solar cell employs a bulk heterojunction active layer—separating photoexcited electrons and holes into distinct materials—and achieves a PCE of 13.3%.¹⁴ However, the device performance is still limited by carrier transport in CQD solids.^{12,15}

Improving the passivation of CQD surfaces and reducing interdot distance enhances transport in CQD films, yet achieving both excellent passivation and small interdot spacing simultaneously remains a challenge.^{4,6,16–22} Initial efforts to improve transport in CQD devices replaced long organic ligands with shorter inorganic ligands using a solid-phase ligand exchange.^{23–26} Ligand exchange was later implemented in the solution phase to improve surface defect passivation, enabling CQD photovoltaics that achieved record performance.⁷ Two-dimensional (2D) matrix engineering further improved the diffusion length by reducing structural and energetic disorder, enhancing the mobility, and further improving performance.⁹ Unfortunately, ionic

Context & Scale

Solution-processed colloidal quantum dots (CQDs) are promising photoelectronic materials for next-generation photovoltaic devices; however, efficient charge transport and surface passivation have yet to be successfully combined in CQD solids. Here, we report a new CQD surface engineering strategy that enables the growth of a monolayer of perovskite that bridges neighboring CQDs, breaking this limitation. The monolayer of perovskite increases interdot coupling, reducing the distance over which carriers must tunnel. The new CQD solids provide fully a 3-fold improvement in mobility relative to the best prior well-passivated CQD solids. As a result, we report a power conversion efficiency (PCE) of 13.8%, a record among PbS CQD solar cells. The study offers an avenue to high-quality semiconducting nanocrystal solids for CQD applications including photodetectors, tandem cells, and light-emitting diodes.

ligands (e.g., PbX_3^- , $\text{X}=\text{I}^-$, Br^- , and Cl^-) cover only surfaces that are charged;^{27,28} charge-neutral surfaces are unprotected, and this leads to fusion of adjacent CQDs. Domains of low-band-gap CQD dimers and clusters act as traps for charge carriers, curtailing both the attainable voltage and the diffusion length.²⁹

Heteroepitaxial growth of perovskite on CQDs has been explored to passivate surface defects and improve device stability.^{15,30–32} However, the resultant thick perovskite matrix is an impediment to interdot charge-carrier transport. The thick (several perovskite crystal unit cells) barrier arises due to the spontaneous nucleation of the perovskite precursors that are incorporated in the CQD ink before assembly.^{15,31,33}

We reasoned that separating adjacent CQDs using a single repeat unit of perovskite (Figure 1)—an approach we term perovskite monolayer bridging—would further decrease the interdot transport barrier while maintaining excellent surface passivation from the epitaxially grown perovskite. Rather than growing the perovskite-CQD solid in a single step by incorporating perovskite precursors into the quantum dot solution, which results in a thick perovskite matrix,¹⁵ we instead devised a self-programmed growth (SPG) strategy to nucleate monolayer perovskite bridges among the QDs.

RESULTS

We prepared CQD films by spin coating a pre-exchanged lead halide-passivated CQD⁷ solution in butylamine (BTA), followed by an annealing step at 70°C for 15 min to remove residual BTA. We then soaked the films in a solution of formamidineium (FA) halide (FAX, $\text{X} = \text{Br}, \text{I}$) in acetonitrile (ACN) (6 mg mL^{-1}) and annealed the films at 70°C for 10 min to form a perovskite matrix around CQDs. We noticed the formation of additional crystals on the surface of the films, so we washed the films with ACN to dissolve these crystals (Figure 1).³⁴

We tracked, using synchrotron grazing-incidence wide-angle X-ray scattering (GI-WAXS) (Figures 2A–2C), perovskite formation before and after the ACN washing. We observed strong perovskite signals (Figure S1A, red mark) from FA bromide (FABr)-treated PbS (FABr-PbS) films before the ACN wash, which indicated the formation of α -FAPbBr $_x$ I $_{3-x}$ after FABr treatment. A weak signal at $q = 0.6 \text{ \AA}^{-1}$ was also observed, which we attribute to a 2D perovskite formed with trace BTA left in the film following annealing.³⁵ After ACN washing, both the signals from α -FAPbBr $_x$ I $_{3-x}$ and from the 2D perovskite almost disappear. The perovskite at the surface is dissolved by ACN (Figures 1 and S2). A weak signal corresponding to the (100) facet of the undissolved perovskite appears at $q = 1.0 \text{ \AA}^{-1}$ due to the limited solubility of perovskite in ACN (Figure S1). We also measured FA iodide (FAI)-treated PbS films after the ACN washing (FAI-PbS) and observed a similar trend (Figure S1B). We studied the films using X-ray diffraction (XRD) (Figure S3) and observed no perovskite signal in either the FAI-PbS or FABr-PbS films after ACN washing. We conclude that the perovskite crystals at the surface were removed with the ACN washing. We also observed that the PbS diffraction signal shifted to lower q values (Figure S1), which we attribute to the tensile strain arising from the perovskite on the PbS surface (Table S1). FABr-PbS films show higher strain than that of FAI-PbS, which we attribute to the improved lattice matching—and increased interfacial bonding strength—of the Br-rich perovskite and the PbS QDs.

We also carried out synchrotron grazing-incidence small-angle X-ray scattering (GISAXS) measurements to track the packing density changes in the CQD films

¹Department of Electrical and Computer Engineering, University of Toronto, 35 St George Street, Toronto, ON M5S 1A4, Canada

²Waterloo Institute for Nanotechnology, University of Waterloo, 200 University Avenue West, Waterloo, ON N2L 3G1, Canada

³X-ray Science Division, Advanced Photon Source, Argonne National Laboratory, Lemont, IL 60439, USA

⁴Division of Physical Sciences and Engineering, King Abdullah University of Science and Technology (KAUST), Thuwal 23955-6900, Saudi Arabia

⁵KAUST Solar Center (KSC), King Abdullah University of Science and Technology (KAUST), Thuwal 23955-6900, Saudi Arabia

⁶Lead Contact

*Correspondence: ted.sargent@utoronto.ca
<https://doi.org/10.1016/j.joule.2020.05.011>

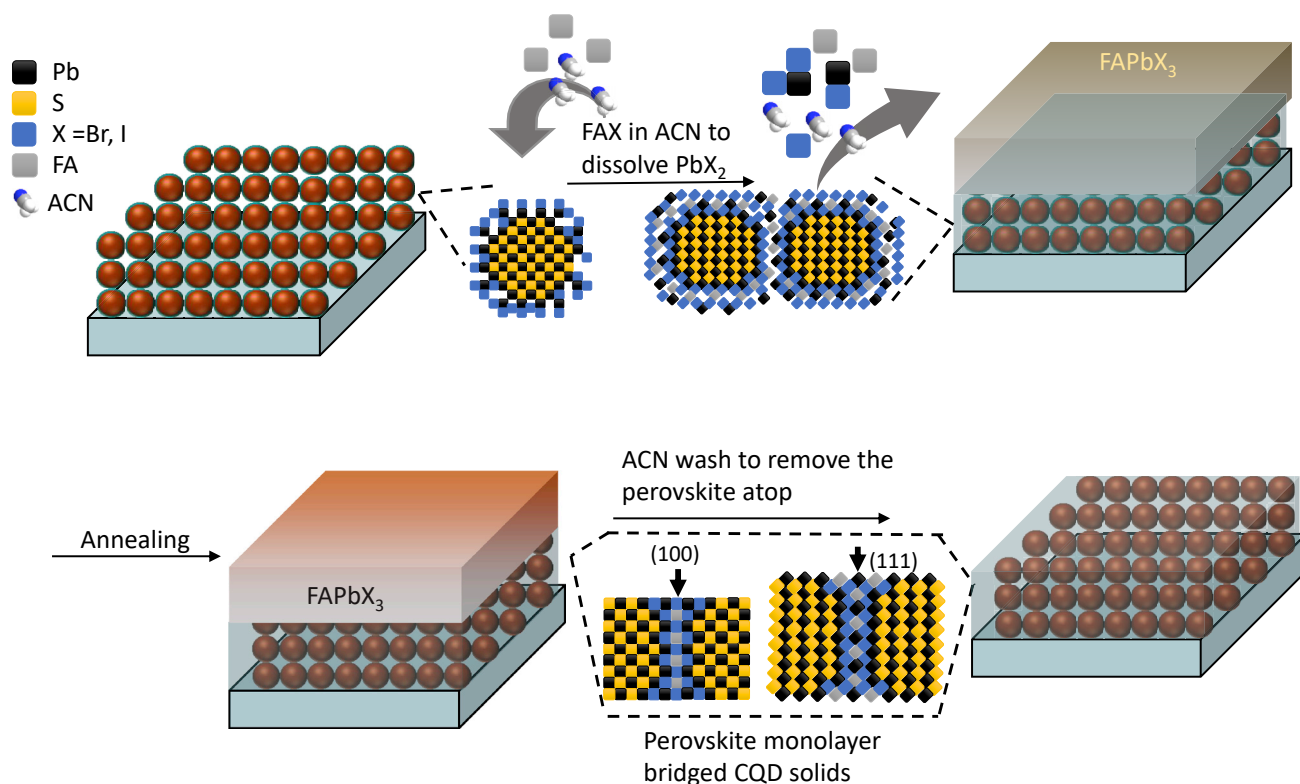


Figure 1. Schematic of the SPG to Form a Monolayer Perovskite Bridge for Strong Coupling and Improved Passivation

The perovskite matrix is formed first by soaking the pre-exchanged CQD films in a FAX ($X = Br, I$) solution, where FAX solution dissolves the PbX_3^- ligands and grow perovskite between adjacent PbS CQDs. The films are annealed and then washed with ACN to remove excess perovskite.

during SPG process (Figures 2D–2F). We found that the interdot distance (between the center of the dots) decreased from 3.35 to 3.20 and 3.15 nm after treatment using FABr and FAI, respectively (Figure 2G). The real part of the refractive index (n) and the imaginary part of the refractive index (κ) are higher in FABr⁻ and FAI⁻ treated CQDs (Figures 2H and 2I), which agrees with the observed reduction in the interdot distance. We also compared the interdot distance before and after the second ACN washing for FABr-PbS (Figure 2G): the unchanged interdot distance indicates that CQD surface ligands are modified during the soaking step and that the ACN washing step does not affect the ligands or the CQD film composition.

We then used high-resolution transmission electron microscopy (HRTEM) to ascertain whether the CQDs are connected by perovskite layers. The real-space images show that CQDs are bridged to one another (Figure 3A), and CQDs are observed to be connected both along the (200) facet (Figure 3B) and the (111) facet (Figure 3C). The lattice spacing at the interface of two CQDs was the same as the spacing within an individual quantum dot, indicating epitaxial alignment at both the (111) and (200) facets. The (111) facet is Pb rich with a positively charged surface, and as a result of the unbalanced stoichiometries, PbS CQDs do not fuse along this direction.^{29,36} In contrast, we did not observe epitaxially fused CQDs in CTL-PbS films (Figure S4). We conclude that a perovskite layer enables the fusion of dots along that direction, and from the uniform lattice spacing throughout the sample, we conclude that the perovskite layer is epitaxially bridging the CQD.

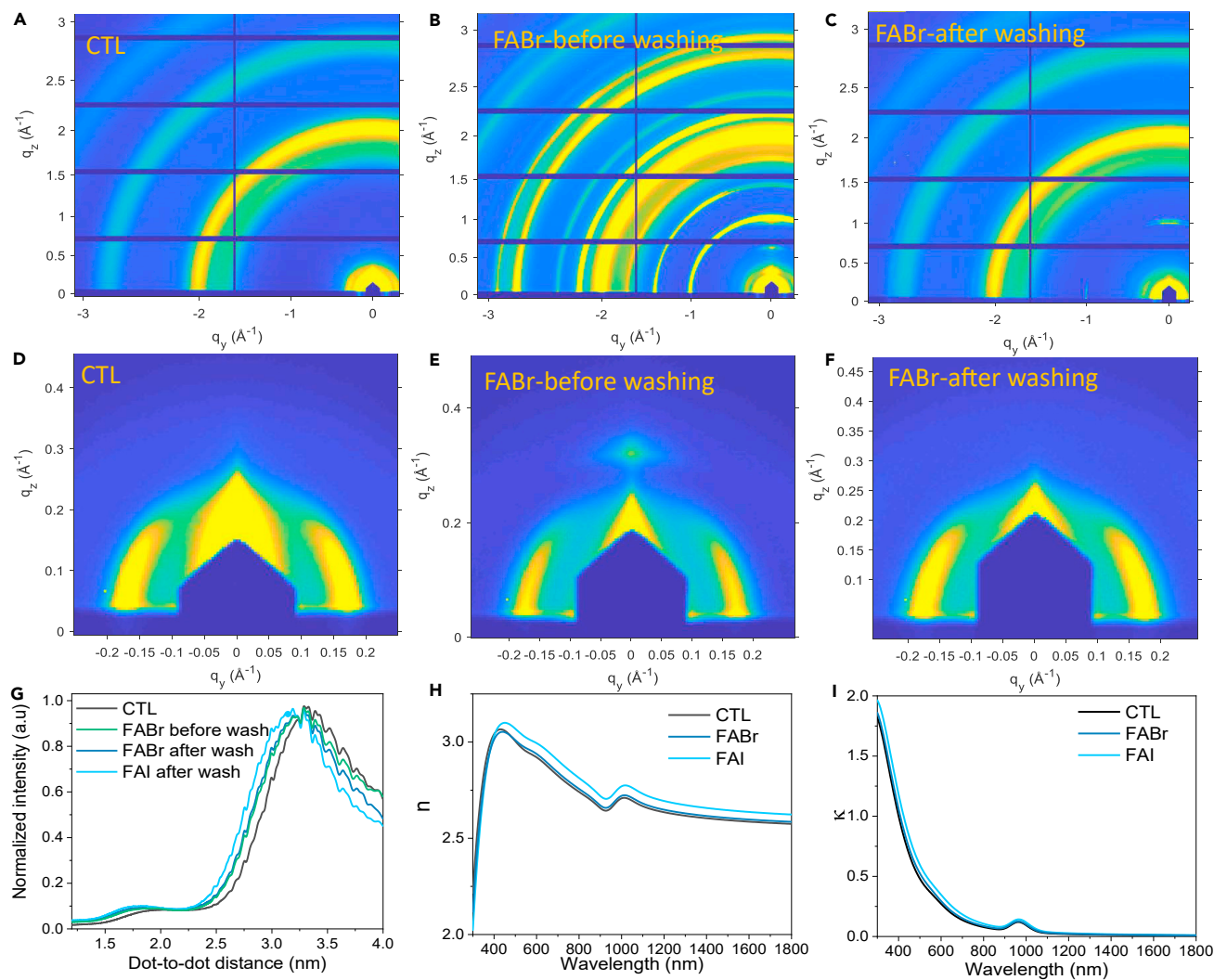


Figure 2. Perovskite Matrix Prepared via FAX Treatment

(A–C) GIWAXS 2D pattern on pristine CQD (CTL) films (A), FABr-treated CQDs (B), and FABr-treated CQDs after acetonitrile (ACN) washing (C); azimuthally integrated intensities (Figure S1) of the diffraction peak show perovskite formation after FABr treatment and removal of perovskite diffraction peaks after washing

(D–F) 2D GISAXS diffraction patterns of pristine CQD (D) and FABr-PbS films before ACN washing (E) and after ACN washing (F). The shift of the patterns to higher q values in (E) and (F) indicates that the interdot spacing (center-to-center) has been reduced.

(G) The interdot spacing is compared as well through azimuthal integration.

(H and I) The real (H) and imaginary (I) refractive index of pristine CQD films, FABr-PbS, and FAI-PbS. The increased real part of the refractive index indicates a higher packing density.

We then directly probed the perovskite in the CQD films (Figure S5) using two-photon ultrafast transient absorption (2PTA). As the perovskite has a significantly larger nonlinear absorption coefficient than PbS,^{37,38} 2PTA offers a means to probe. We excited the CQD films using an 1,100 nm pulse laser and collected the transient absorption (TA) bleach signal at ~ 600 nm (perovskite absorption). We observed strong absorption bleach between 550 and 750 nm for FABr-PbS films before ACN wash. The strong signal is attributed to the crystals that are observed at the surface of the film. We also observed a positive peak at shorter wavelengths, which is attributed to the light-induced activation of the forbidden exciton transition.^{35,39} After washing with ACN, the bleach peak that we observed from perovskite was blue

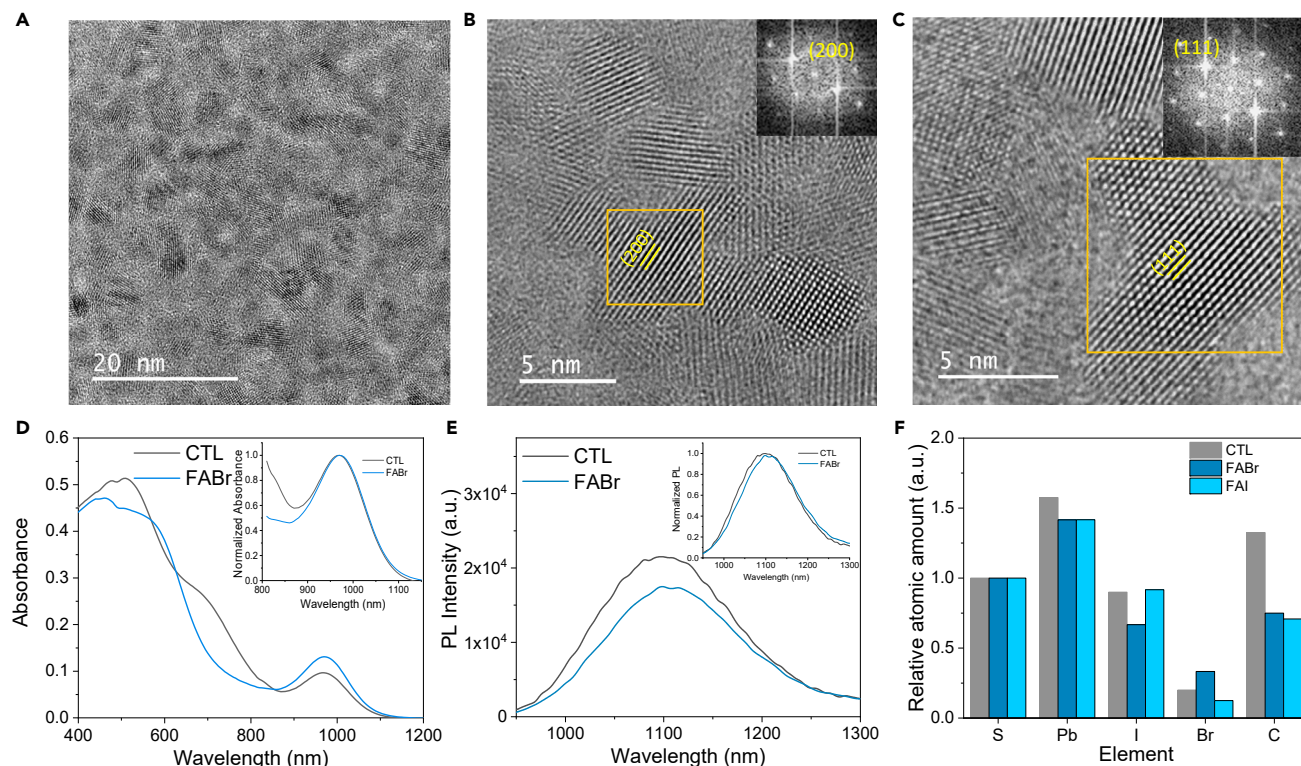


Figure 3. CQDs Connected via Monolayer Perovskite Bridges

(A) HRTEM micrograph of FABr-PbS CQDs after ACN wash.

(B and C) HRTEM micrograph of an epitaxial CQD cluster connected along the (200) facet (B) and the (111) facet (C). Lattice fringes of 3.0 ± 0.1 and 3.4 ± 0.1 Å spacing are ascribed to (200) and (111) planes. The inset of each image shows the selected-area electron diffraction (SAED) image.

(D) Absorbance (Abs) of CQD films before and after FABr treatment: the FABr-PbS films show a larger peak-to-valley ratio and a slight blueshift compared with the pristine PbS CQD films.

(E) PL measurements show slightly decreased PL intensity which may be due to faster exciton dissociation and improved mobility.

Insets in (D) and (E) show normalized absorption spectra.

(F) Elemental ratios from RBS measurements. The CTL-PbS films are found to have $\sim 1.58:1$ atomic ratio of Pb:S, whereas FABr-PbS and FAI-PbS films show a decreased Pb:S ratio of $\sim 1.41:1$.

shifted to 570 nm (Figure S6). We attribute the blueshift to excitonic confinement that is present in a monolayer of perovskite.³⁵ After ~ 2 ps, the bleach signal observed at the perovskite absorption edge disappeared as the generated carriers were transferred into the PbS CQD. We did not observe bleach signal around at 600 nm but at ~ 950 nm (PbS QD band edge), which we attribute to the ground-to-trap-state transition excited by 1,100 nm.

We sought further evidence that either confirmed or refuted the view that the CQDs were connected by a thin perovskite layer. Absorbance (Figure 3D) and photoluminescence (PL) (Figure 3E) showed that quantum confinement is preserved after the perovskite is grown and the interdot spacing is decreased.⁴⁰ If the CQDs were fusing directly, the increased size would result in a substantial redshift in both the absorption and emission of the film.²⁹ The <5 nm redshifts of the absorption and PL spectra indicated that the CQDs, despite being connected, remain energetically confined. The FABr-PbS films also showed a higher peak-to-valley absorption ratio at the excitonic wavelength. However, the PL intensity decreased slightly after FABr treatment, which we attribute to the improved interdot electric coupling and thus faster exciton dissociation.⁴¹ We observed similar results following FAI treatment (Figure S7).

Based on this, we conclude that a high-band-gap perovskite separates the CQDs and preserves the quantum confinement by forming a type I heterojunction (Figure S8).

To determine the thickness of perovskite bridge in CQD films, we then carried out Rutherford backscattering spectroscopy (RBS) (Figure S9). RBS ratios are tabulated in Table S2, in which each value was normalized to the S signal. The RBS results revealed that the Pb:S molar ratio decreased from $\sim 1.58:1$ to $\sim 1.41:1$ after FAX treatment (Figure 3F). This indicates that the excess Pb (from the Pb halide ligands used to passivate the CQDs) was removed by the treatment, which is expected from the smaller interdot spacing in the treated dots. We also observed a reduced fraction of C in FAX-treated films, indicating that BTA was more efficiently removed.

From previous reports on PbS CQDs (band gap 1.3 eV),⁴² we were able to identify the chemical environment of the PbS CQDs (Table S2; Supplemental Experimental Procedures). Additionally, we know from RBS the amount of Br and I that are present in the system and the passivated CQD should be charged neutral, enabling us to estimate the amount of FA present. We found that the amount of FA (reported as a molar ratio to the total sulfur atoms in the sample), $\text{Pb}_{\text{ligand}}$, and halides (X^-) in the FABr-PbS and FAI-PbS samples were just enough to form the perovskite monolayer bridging QDs by FAPb_2I_5 along (100) facets and FAPbX_7 along (111) facets (Figure S6; Table S2). This indicates that the ligands on the CQD surface form on average ~ 1 layer of perovskite surrounding the surface of each quantum dot, since each perovskite unit cell passivates 2 CQD unit cells (Figure 1).

Taken together with the 2PTA, the PL and absorption spectra, the strain in the PbS QDs, and HRTEM images showing epitaxial lattice matching, the studies suggest that approximately a monolayer of perovskite, composed of one layer of FA and two layers of Pb (Figure 1), bridges the quantum dots. We postulate that this is enabled by lattice anchoring from the PbS surface: the FAX/ACN solution efficiently dissolves any free-standing perovskite, as well as PbX_2 (as shown in Figure S2), possibly through an intermediate step of its conversion into perovskite, and lattice anchoring¹⁵ to adjacent PbS surfaces on both sides of the monolayer of perovskite stabilizes the perovskite and prevents from dissolving. Utilizing this disparity in solubilities allows tuning the treatment conditions to retain single monolayers while fully dissolving any double-layer perovskite.

We sought to investigate whether the perovskite bridge impacts charge transport.⁴³ We estimated carrier mobility with ultrafast TA spectroscopy (TAS) (Figure S10). The FAI-PbS and FABr-PbS films show a $\sim 300\%$ higher mobility than the CTL-PbS film (Figure 4A). The mobilities are also $\sim 40\%$ higher than those of previously reported PbS CQD films protected with thick perovskite shells,¹⁵ which we attribute to the decreased perovskite matrix thickness. We obtained lifetimes from a microsecond TA setup (Experimental Procedures). Each decay trace was fit to a biexponential curve: the carrier lifetimes of the CTL-PbS, FABr-PbS, and FAI-PbS films were found to be 66 ± 2 , 72 ± 3 , and 78 ± 3 ns, respectively (Figure 4B; Table S3), which, when combined with the mobility, yielded a 4-fold higher mobility-lifetime product for FAX-PbS films (Figure 4C). The FAX-PbS films had a diffusion length that was $\sim 2\times$ longer than the CTL-PbS films.

We also investigated mobility using time-resolved terahertz spectroscopy (TRTS).⁴⁴ Figure 4D shows the time-resolved terahertz photoconductivity for each of the films. Mobility and lifetime values were extracted from the traces (Figure S11): FABr-PbS

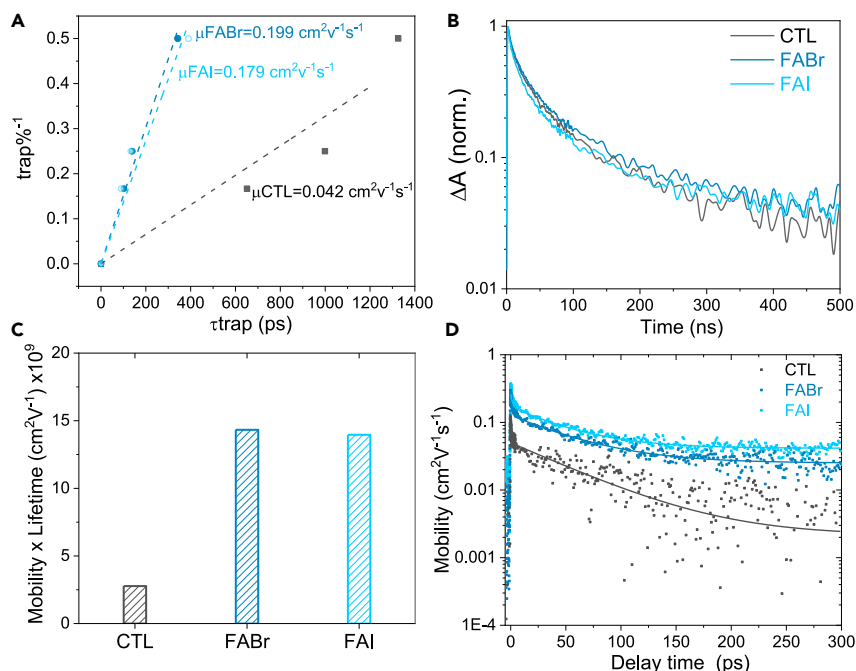


Figure 4. Improved Mobility and Electric Coupling Using Perovskite Monolayer Bridges

(A) Carrier mobility determined via TA spectroscopy. CTL-PbS, FABr-PbS, and FAI-PbS films have mobilities of ~ 0.04 , ~ 0.20 , and ~ 0.18 $\text{cm}^2\text{V}^{-1}\text{s}^{-1}$, respectively.

(B) Microsecond TA decay of the bleach intensity for each film: the carrier lifetimes are extracted from biexponential fits (Table S3), where the short lifetime component is ~ 10 ns, and the long components of the CTL-PbS, FABr-PbS, and FAI-PbS films are 66 ± 2 , 72 ± 3 , and 78 ± 3 ns, respectively.

(C) Comparison of TA carrier mobility $\mu \times$ lifetime τ product.

(D) Time-resolved terahertz photoconductivity measurements of the films of CTL-PbS film (black) compared with FABr-PbS films (dark blue) along with FAI-PbS film (light blue).

and FAI-PbS had mobility values of ~ 0.37 and ~ 0.30 $\text{cm}^2\text{V}^{-1}\text{s}^{-1}$, respectively. This is $2\times$ higher than that of the CTL-PbS film (~ 0.12 $\text{cm}^2\text{V}^{-1}\text{s}^{-1}$), in agreement with the mobilities extracted from the TA spectra. FABr-PbS showed slightly higher mobility than that of FAI-PbS in both TA and TRTS methods, which we attribute to the increased surface passivation due to the smaller lattice mismatch between PbS and FAPbBr₃ perovskite.

Seeking to lever the improved diffusion length, we fabricated FABr-PbS CQD solar cells (Figure 5B).⁸ We used time-of-flight secondary ion mass spectrometry (TOF-SIMS) (Figure S12) to profile the FA distribution in the active layer: the FA and PbI⁺ signals remained constant over the entirety of the ~ 440 nm film, indicating that FAPbI_xBr_{3-x} was evenly distributed through the FABr-PbS solid.

When we optimized device thickness, the improved mobility enabled thicker PV devices, and at the same time, the increased passivation enhanced open-circuit voltage (V_{OC}) and fill factor (FF) simultaneously (Figure S13). The short circuit current density (J_{SC}) for CTL-PbS devices was lower than FABr-PbS-based devices at all active-layer thicknesses. The FF s of FABr-PbS devices were over 70% for the thicknesses below 440 nm, which significantly improved compared with CTL-PbS films; the FF s obtained here were also higher than those previously reported PV devices based on solution-exchanged PbS CQDs.^{7-9,15}

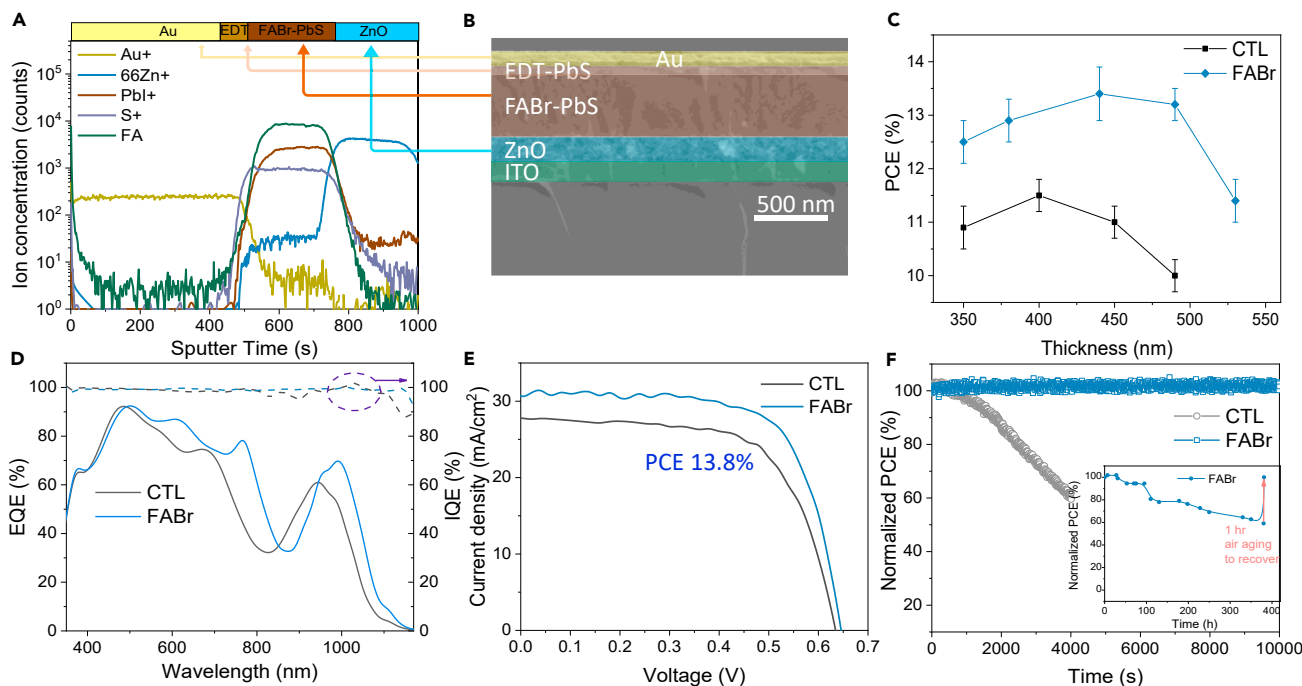


Figure 5. Photovoltaic Performance of Control versus Bridged Films

(A) TOF-SIMS depth profile of FABr-PbS solar cell device showing that FA (CH_5N_2^+) is evenly distributed throughout.

(B) Cross-section scanning electron microscopy (SEM) image of a typical device structure.

(C) Active-layer thickness-dependent PCE for CTL-PbS and FABr-PbS films. The optimal FABr-PbS devices are 50 nm thicker than devices made using untreated dots.

(D) EQE and IQE spectra.

(E) J - V curves of champion devices for treated and untreated CQDs.

(F) Stability unencapsulated devices operating at the MPP under continuous AM1.5G illumination. FABr-PbS devices show no degradation for 2.8 h (then gradually reduced to approximately 60% in 380 h [inset]), whereas CTL-PbS devices degrade to 60% of the initial PCE after 1.1 h.

The optimum active-layer thickness for FABr-PbS devices was found to be 440 nm. The devices showed reproducibly high performance, with a champion PCE of 13.8% without hysteresis (Figures 5C and S14): the V_{OC} , J_{SC} , and FF of the optimal FABr-PbS-based devices were 0.65 V, 30 mA cm^{-2} , and 71%, respectively. The best CTL-PbS device had a PCE of 11.8%, with a V_{OC} , J_{SC} , and FF of 0.63 V, 28 mA cm^{-2} , and 67%, respectively. The perovskite monolayer bridge strategy provides increased PCE due to improved charge transport and increased FF and J_{SC} as opposed to previous strategies that led to the formation of excessively thick perovskite (best PCE is 12.6%),¹⁵ hindering electrical coupling. The J_{SC} values obtained from the J - V curves were consistent with the external quantum efficiency (EQE) integrated J_{SC} (Figure 5D): the integrated J_{SC} values for FABr-PbS and CTL films were 29 and 26 mA cm^{-2} , respectively. The internal quantum efficiency (IQE), which was obtained by dividing the EQE at 0 V by the EQE at -2 V, indicates that FABr-PbS devices have an IQE near unity over the entire spectra range, whereas the CTL-PbS devices have lower IQE over the range 600–1,100 nm. The AM1.5 PCE from an accredited laboratory (Newport) shows a PCE of 12.43% \pm 0.32% (Figure S15).

The improved surface passivation and lattice anchoring between PbS and perovskite¹⁵ also enhance operating stability, retaining 100% of the initial PCE following 2.8 h of continuous AM1.5G illumination in nitrogen (Figure 5F) and then gradually decreasing to approximately 60% in 380 h (Figure 5F inset). The device performance

recovered after aging in air for ~ 1 h to p-dope the EDT layer, suggesting that the PbS active layer is stable during maximum power point (MPP) operation. The CTL-PbS devices degraded to 60% of the initial PCE value within 1.1 h, indicating that the perovskite matrix improves surface passivation, in agreement with previous results.^{9,15} Histograms of controls and FABr-PbS device PCE (Figure S16) showed reproducible performance. We compared the thermal stability of the active layer by fabricating the PbS active layer annealed at different temperatures (Figure S17): the FABr-PbS devices showed constant V_{OC} and FF annealed at 70°C and 100°C, whereas the CTL-PbS devices showed decreased V_{OC} and FF at higher annealing temperatures. This indicates that the epitaxial perovskite shells prevent CQD fusion.

We also studied FAI-PbS PV devices, which show an optimal PCE of 13.4% (Figure S18). However, the devices degraded to 90% of their initial PCE after 3 days storage in air, which we attribute to the unstable α -FAPbI₃ and the interfacial strain that was induced by the large lattice mismatch between FAPbI₃ and PbS.

We also found that methylammonium iodide (MAI) treatment improved the PCE (Figure S19) by increasing FF and J_{SC} but decreased the V_{OC} . This may be due to the aggressive stripping of PbX₃⁻ by MAX.³⁴

DISCUSSION

In summary, we present a new SPG strategy to improve both surface passivation and packing density of CQDs. Through the growth of a monolayer of perovskite on CQD surfaces, we obtain CQD films with increased mobility and improved stability relative to the halide-passivated CQD films. The enhanced mobility and passivation facilitate the use of a thick photoactive layer in solar cell devices, delivering an improved efficiency by increasing V_{OC} , J_{SC} , and FF simultaneously. More broadly, this study provides a new avenue to form high-quality semiconducting nanocrystal solids for the wide CQD applications, such as photodetectors, tandem cells, and light-emitting diodes.

EXPERIMENTAL PROCEDURES

Resource Availability

Lead Contact

Further information and requests for resources and materials should be directed to and will be fulfilled by the Lead Contact, Edward H. Sargent (ted.sargent@utoronto.ca).

Materials Availability

The materials generated in this study will be made available on reasonable request.

Data and Code Availability

Supporting data of this study will be made available on reasonable request.

Materials

PbO, PbBr₂ (99.9%), and PbI₂ (99.9%) were purchased from Alpha Aesar. N,N-dimethylformamide (DMF, anhydrous), toluene, octane, oleic acid (>99%), and ammonium acetate (AA) were purchased from Sigma-Aldrich. FABr and FAI were purchased from Great Cell Solar. All chemicals were used as procured without further purification.

CQD Synthesis and Solution Ligand Exchange

PbS CQDs were synthesized and washed according to previous reports.⁴⁵ A ligand exchange process was carried out in the solution phase in ambient conditions. The

exchange solution was prepared (PbI_2 0.1 M, PbBr_2 0.04 M, and AA 0.04 M) in DMF. 5 mL of as-synthesized PbS QDs octane solution (10 mg mL^{-1}) was added to 5 mL of precursor solution, followed by vigorous mixing for 2 min until the QDs completely transferred to the DMF phase. The DMF phase was then washed three times by vigorous mixing with 5 mL of octane for 30 s, followed by the addition of 3 mL of toluene and finally centrifuging at 3,300 rpm for 1 min (precipitate collected). The solids were then dried for 15 min in the vacuum antichamber of a glovebox.

Film Fabrication

The dried QD solids were redispersed in BTA ($300\text{--}400 \text{ mg mL}^{-1}$) for film by spin coating at a spin rate from 1,500 to 2,500 rpm in air, followed by annealing at 70°C for 15 min in N_2 filled glovebox to remove solvent residues. Then the as-prepared films were soaked in FAI/FABr solution (6 mg mL^{-1} in ACN) and spin to dry at 2,000 rpm for 20 s. The film was then annealed at 70°C for 10 min in N_2 filled glovebox to crystallize the perovskite matrix. After cooling down to room temperature, the QD film was washed by drop-casting ACN on the surface. The QD film was finally dried at 70°C for 5 min in N_2 filled glovebox.

X-Ray Scattering Measurements

Both GIWAXS and GISAXS measurements were performed at beamline 8-ID-E, Advanced Photon Source, Argonne National Laboratory, with 10.86 KeV incident X-rays and a Pilatus 1M detector 228 mm from the samples. To reduce radiation damage, all samples were mounted in a vacuum chamber. The scattering patterns were obtained at a photon-incident angle of 0.18 degrees with respect to the sample plane, and the exposure times were 30 s.

Samples for GISAXS and GIWAXS were spin coated on Si substrates following the same SPG procedures used in film fabrication.

XRD Measurements

QD films were made using the abovementioned SPG process and measured using a Rigaku MiniFlex 600 diffractometer equipped with a NaI scintillation counter and using a monochromatized Copper $K\alpha$ radiation ($\lambda = 1.5406 \text{ \AA}$).

HRTEM Measurements

HRTEM analysis was carried out with a Titan TEM (FEI Company) operating at a beam energy of 300 keV and equipped with a Tridiem post-column energy filter (Gatan). Samples for TEM were spin coated the QDs in BTA (4 mg mL^{-1}) solution on an ultrathin-carbon film (Ted Pella 01800-F), following the same SPG process in film fabrication.

SEM Measurements

The cross-section image of the device was investigated using a Hitachi SU8230 SEM.

Absorption and PL Measurements

Optical absorption measurements were performed on a Lambda 950 UV-vis-IR spectrometer. PL measurements were carried out with a Horiba Fluorolog time-correlated single-photon counting system equipped with UV-vis-NIR photomultiplier tube detectors, dual grating spectrometers, and a monochromatized xenon lamp excitation source.

2PTA Spectroscopy

Femtosecond laser pulses of an 1,100 nm beam at a 5 kHz repetition rate were produced using a regeneratively amplified Yb:KGW laser (PHAROS, light conversion). Both the pump and probe pulses were directed into a commercial transient absorption spectrometer (Helios, ultrafast). Delaying the probe pulse relative to the pump provides a time window of up to 8 ns, and the time resolution of these experiments was 200 to 300 fs (estimated by the rise time of signal amplitudes in transient absorption spectra). Samples were prepared on glass. All measurements were performed using an average power of 10 mW with a spot size of 400 μm^2 .

Extraction of Mobility from TAS

Charge-carrier mobilities were obtained with the aid of ultrafast TAS. The amplitude of the band-edge bleach signal in TAS is representative of the band-edge carrier population. When small-band-gap carrier-acceptor CQDs were added to large-band-gap carrier-donor CQDs at given concentrations (N_t), the change in donor CQD lifetime (τ) with varying N_t of acceptor CQDs provides the diffusion coefficient (D) and mobility (μ).

$$D = \frac{d}{6\sigma \left(\tau / N_t^{-1} \right)}$$

σ is the capture cross-section, which for the 3D model is assumed to be $1/4 \pi d^2$. Population transfer can be monitored directly by tracking the decay in the donor CQD bleach signals (Figure S10). When N_t^{-1} is plotted against τ , the resulted slope is proportional to the mobilities of carriers.

A chopper was used to block every other pump pulse. Each probe pulse was measured by a CCD after dispersion by a grating spectrograph (ultrafast, Helios). A regeneratively amplified Yb:KGW laser (PHAROS, light conversion) laser was used to generate femtosecond pulses (250 fs FWHM) at 1,030 nm as the fundamental beam with a 5 kHz repetition rate. This fundamental beam was passed through a beam-splitter, where one arm was used to pump an optical parametric amplifier (ORPHEUS, light conversion) for the narrowband pump, and the other arm was focused into a sapphire crystal (ultrafast systems) to generate a NIR white-light continuum probe with a spectral window of 900 to 1,000 nm. Both arms were directed into a commercial transient absorption spectrometer (Helios, ultrafast systems). The probe pulse was delayed relative to the pump pulse to provide a time window of up to 7 ns. Samples were prepared on glass substrates and translated at 1 mm s^{-1} during the measurement. All measurements were performed using an average power of 60 μW with a spot size of 0.40 μm^2 , assuming a Gaussian beam profile. Kinetic traces were fit to the convolution of the instrument response and a sum of exponential decays. Time zero could vary with wavelength to account for the chirp of the probe.

Microsecond TA

TAS was carried out using a homebuilt pump-probe setup. The output of titanium:sapphire amplifier (Coherent Legend DUO, 4.5 mJ, 3 kHz, 100 fs) was attenuated and focused on a c-cut 3 mm thick sapphire window, thereby generating a white-light supercontinuum from 500 to 1,600 nm (probe pulse). The excitation light (pump pulse) was provided by an actively Q-switched Nd:YVO₄ laser (InnoLas piccolo AOT) frequency doubled to provide pulses at 532 nm. The pump laser was triggered by an electronic delay generator (Stanford research systems DG535) itself

triggered by the transistor-transistor logic (TTL) sync from the Legend DUO, allowing control of the delay between pump and probe with a jitter of roughly 100 ps. Pump and probe beams were focused on the sample that was kept under a dynamic vacuum of $10\text{--}5\text{ mbar}$. The transmitted fraction of the white light was guided to a custom-made prism spectrograph (Entwicklungsbüro Stressing) where it was dispersed by a prism onto a 512-pixel complementary metal-oxide-semiconductor (CMOS) linear image sensor (Hamamatsu G11608-512DA). The probe pulse repetition rate was 3 kHz, while the excitation pulses were mechanically chopped to 1.5 kHz (100 fs to 8 ns delays) or directly generated at 1.5 kHz frequency (1 ns to 300 μs delays), while the detector array was read out at 3 kHz. Adjacent diode readings corresponding to the transmission of the sample after excitation and in the absence of an excitation pulse, respectively, were used to calculate $\Delta T/T$. Measurements were averaged over several thousand shots to obtain a good signal-to-noise ratio. The chirp induced by the transmissive optics was corrected with a homebuilt MATLAB code. The delay at which pump and probe arrive simultaneously on the sample (i.e., zero time) was determined from the point of maximum slope (fastest raise) of the TA signal.

Mobility Calculation from TRTS Measurements

TRTS setup is based on an amplified Ti:sapphire laser which outputs a train of short pulses with around 100 fs pulse width and 800 nm central wavelength at a repetition rate of 1,040 Hz. The output is split into two beam paths: one for pumping the sample and one for generating and detecting THz pulse via ZnTe (110) crystals. To ensure the pumping beam is uniformly focused onto the sample at the same area of the THz beam, a home-made metal plate with a pinhole of 1.5 mm in diameter is used to control the apertures of both THz and pumping beams. To minimize the absorption of THz beam from the atmosphere, the entire THz optical path is placed inside a vacuumed chamber.

In TRTS measurements, the change in the peak THz time-domain transmission is recorded as a function of the time delay between the THz pulse and pumping pulse onto the sample. The pumping pulse is set with a fluence of 4.58×10^{15} photons/ cm^2 per pulse. The mobility and carrier lifetimes of the thin films are proportional to the change in the peak of THz-time-domain transmission, which is calculated by the following relationship:

$$\mu_s \cdot f_s(\tau) = \left[\frac{(1 + n_s)c\epsilon_0}{e \cdot J_{abs}} \right] \left[\frac{\Delta E(\tau)}{E} \right],$$

where absorbed fluence J_{abs} is calculated by

$$J_{abs} = J_{incident}(1 - R) - J_{transmitted}.$$

The reflectance R of each thin film sample is calculated through the measured refractive index data (Fresnel equation)

While the transmitted power is measured at the backside of the mounted sample.

μ_s is the sum of the electron mobility and hole mobility.

TOF-SIMS

TOF-SIMS was performed using ToF-SIMS5 from ION-TOF GmbH (Munster, Germany). Samples were analyzed in dual beam profiling mode. All profiles were performed in non-interlaced mode. Spectral data were acquired in a high mass-resolution mode. The primary ion for analysis was 30keV Bi^{3+} at 0.3 pA (Bi liquid metal ion

source). This ion beam was applied over a $100 \times 100 \mu\text{m}$ area at the center of the sputter center. The sputter ion was 1keV Ar⁺ at 120 nA (Ar, electron impact ion source).

CQD Solar Cell Fabrication

ZnO layer was adopted as an electron acceptor layer and formed on a patterned ITO-coated glass substrate by spin coating 2 layers of ZnO nanoparticles solution at 5,000 rpm for 30 s. Then CQD solid films were obtained following the film fabrication process above, followed by two layers of EDT-exchanged PbS CQDs as follows: 50 μL of oleic acid-capped PbS CQDs (exciton peak at 850 nm) octane solution (50 mg mL^{-1}) were spin coated at 2,500 rpm for 10 s, followed by soaking in 0.01% EDT in ACN (ACN) solution for 30 s and washing with ACN for 3 times. Then 120 nm of Au was deposited on EDT PbS CQD film as a back electrode.

AM 1.5G Solar Efficiency Measurement

The active area (0.049 cm^2) was determined by the aperture placed between the solar cell and the AM1.5G solar simulator (Sciencetech class A). Through this aperture, the light intensity (1 sun, 100 mW cm^{-2}) was calibrated using a Melles Griot broadband power meter. The spectral mismatch was calibrated using a reference solar cell (Newport). The $J-V$ curve was measured by a Keithley multimeter by scanning the bias forward (-0.7 to 0.1 V) and backward (0.1 to -0.7 V). The device stability was measured by fixing the bias at the maximum power output point determined from $J-V$ curves.

External and Internal Quantum Efficiency

EQE and IQE spectra were acquired on a QuantX-300 quantum efficiency measurement system (Newport). Monochromated white light from a xenon lamp was mechanically chopped at a frequency of 25 Hz. EQE spectra were acquired at zero electrical bias, whereas IQE spectra were calculated from EQE spectra taken at a negative bias of -2 V using the following formula: $\text{IQE} = \text{EQE}(0 \text{ V})/\text{EQE}(-2 \text{ V})$.

SUPPLEMENTAL INFORMATION

Supplemental Information can be found online at <https://doi.org/10.1016/j.joule.2020.05.011>.

ACKNOWLEDGMENTS

This work was supported by Ontario Research Fund-Research Excellence program (ORF7-Ministry of Research and Innovation, Ontario Research Fund-Research Excellence Round 7), and by the King Abdullah University of Science and Technology (KAUST) Office of Sponsored Research (OSR) under award no. OSR-2018-CRG7-373702 and award no. OSR-2018-CARF/CCF-3079. This work used resources of the Advanced Photon Source, a U.S. Department of Energy (DOE) Office of Science User Facility operated for the DOE Office of Science by Argonne National Laboratory under contract no. DE-AC02-06CH11357. We thank A.R. Kirmani for GISAXS and GIWAXS discussions. We thank L. Goncharova for assistance with RBS measurements. We thank A.H. Proppe, L. Chiluka, Y. Hou, M. Biondi, Y. Wang, M. Vafaei, and G. Bappi for manuscript discussion. We thank D. Kopilovic, E. Palmiano, L. Levina, and R. Wolowiec for technical support.

AUTHOR CONTRIBUTIONS

B.S. conceived the idea of this study; B.S. developed the perovskite monolayer CQD system, fabricated and characterized solar cell devices, and performed SIMS and

materials stability tests; O.V. assisted in RBS measurements and analysis; M.W. assisted in the fabrication of quantum dot in matrix samples and absorption and photoluminescence measurements; A.J., Y.G., and F.L. carried out transient absorption measurements and data analysis; Z.J. and H.Z. carried out GISAXS and GIWAXS measurements; X.Z., J.L., O.M.B., and Y.G. assisted the HRTEM measurements; C.X. and D.B. carried out the TRTS measurement and mobility extraction; M.-J.C. performed SEM imaging measurements; Y.D. assisted in 2PTA measurement; S.-W.B. assisted device preparation for certification; and F.P.G.d.A. and E.H.S. supervised the project. B.S., A.J., F.P.G.d.A., and E.H.S. wrote the manuscript, and all authors discussed the results and assisted in the preparation of the manuscript.

DECLARATION OF INTERESTS

The authors declare no competing interests.

Received: February 5, 2020

Revised: March 31, 2020

Accepted: May 13, 2020

Published: June 9, 2020

REFERENCES

- Murray, C.B., Norris, D.J., and Bawendi, M.G. (1993). Synthesis and characterization of nearly monodisperse CdE (E = sulfur, selenium, tellurium) semiconductor nanocrystallites. *J. Am. Chem. Soc.* *115*, 8706–8715.
- Yu, W.W., Wang, Y.A., and Peng, X. (2003). Formation and stability of size-, shape-, and structure-controlled CdTe nanocrystals: ligand effects on monomers and nanocrystals. *Chem. Mater.* *15*, 4300–4308.
- Murray, C.B., Kagan, C.R., and Bawendi, M.G. (2000). Synthesis and characterization of monodisperse nanocrystals and close-packed nanocrystal assemblies. *Annu. Rev. Mater. Sci.* *30*, 545–610.
- Sargent, E.H. (2012). Colloidal quantum dot solar cells. *Nat. Photon.* *6*, 133–135.
- Park, Y.I., Piao, Y., Lee, N., Yoo, B., Kim, B.H., Choi, S.H., and Hyeon, T. (2011). Transformation of hydrophobic iron oxide nanoparticles to hydrophilic and biocompatible maghemite nanocrystals for use as highly efficient MRI contrast agent. *J. Mater. Chem.* *21*, 11472–11477.
- Kagan, C.R., Lifshitz, E., Sargent, E.H., and Talapin, D.V. (2016). Building devices from colloidal quantum dots. *Science* *353*, aac5523.
- Liu, M., Voznyy, O., Sabatini, R., García de Arquer, F.P., Munir, R., Balawi, A.H., Lan, X., Fan, F., Walters, G., Kirmani, A.R., et al. (2017). Hybrid organic-inorganic inks flatten the energy landscape in colloidal quantum dot solids. *Nat. Mater.* *16*, 258–263.
- Sun, B., Voznyy, O., Tan, H., Stadler, P., Liu, M., Walters, G., Proppe, A.H., Liu, M., Fan, J., Zhuang, T., et al. (2017). Pseudohalide-exchanged quantum dot solids achieve record quantum efficiency in infrared photovoltaics. *Adv. Mater.* *29*, 1700749.
- Xu, J., Voznyy, O., Liu, M., Kirmani, A.R., Walters, G., Munir, R., Abdelsamie, M., Proppe, A.H., Sarkar, A., García de Arquer, F.P., et al. (2018). 2D matrix engineering for homogeneous quantum dot coupling in photovoltaic solids. *Nat. Nanotechnol.* *13*, 456–462.
- Kim, J., Ouellette, O., Voznyy, O., Wei, M., Choi, J., Choi, M.J., Jo, J.W., Baek, S.W., Fan, J., Saidaminov, M.I., et al. (2018). Butylamine-catalyzed synthesis of nanocrystal inks enables efficient infrared CQD solar cells. *Adv. Mater.* *30*, e1803830.
- Chuang, C.H., Brown, P.R., Bulović, V., and Bawendi, M.G. (2014). Improved performance and stability in quantum dot solar cells through band alignment engineering. *Nat. Mater.* *13*, 796–801.
- Baek, S.-W., Jun, S., Kim, B., Proppe, A.H., Ouellette, O., Voznyy, O., Kim, C., Kim, J., Walters, G., Song, J.H., et al. (2019). Efficient hybrid colloidal quantum dot/organic solar cells mediated by near-infrared sensitizing small molecules. *Nat. Energy* *4*, 969–976.
- Yang, Z., Fan, J.Z., Proppe, A.H., Arquer, F.P.G., Rossouw, D., Voznyy, O., Lan, X., Liu, M., Walters, G., Quintero-Bermudez, R., et al. (2017). Mixed-quantum-dot solar cells. *Nat. Commun.* *8*, 1325.
- Choi, M.J., García de Arquer, F.P., Proppe, A.H., Seifitokaldani, A., Choi, J., Kim, J., Baek, S.W., Liu, M., Sun, B., Biondi, M., et al. (2020). Cascade surface modification of colloidal quantum dot inks enables efficient bulk homojunction photovoltaics. *Nat. Commun.* *11*, 103.
- Liu, M., Chen, Y., Tan, C.S., Quintero-Bermudez, R., Proppe, A.H., Munir, R., Tan, H., Voznyy, O., Scheffel, B., Walters, G., et al. (2019). Lattice anchoring stabilizes solution-processed semiconductors. *Nature* *570*, 96–101.
- Lee, J.S., Kovalenko, M.V., Huang, J., Chung, D.S., and Talapin, D.V. (2011). Band-like transport, high electron mobility and high photoconductivity in all-inorganic nanocrystal arrays. *Nat. Nanotechnol.* *6*, 348–352.
- Scalise, E., Srivastava, V., Janke, E., Talapin, D., Galli, G., and Wippermann, S. (2018). Surface chemistry and buried interfaces in all-inorganic nanocrystalline solids. *Nat. Nanotechnol.* *13*, 841–848.
- Zhang, H., Dasbiswas, K., Ludwig, N.B., Han, G., Lee, B., Vaikuntanathan, S., and Talapin, D.V. (2017). Stable colloids in molten inorganic salts. *Nature* *542*, 328–331.
- Kovalenko, M.V. (2015). Opportunities and challenges for quantum dot photovoltaics. *Nat. Nanotechnol.* *10*, 994–997.
- Talapin, D.V., and Murray, C.B. (2005). PbSe nanocrystal solids for n- and p-channel thin film field-effect transistors. *Science* *310*, 86–89.
- Yuan, M., Liu, M., and Sargent, E.H. (2016). Colloidal quantum dot solids for solution-processed solar cells. *Nat. Energy* *1*, 16016.
- Saran, R., and Curry, R.J. (2016). Lead sulphide nanocrystal photodetector technologies. *Nat. Photonics* *10*, 81–92.
- Shen, T., Li, B., Zheng, K., Pullerits, T., Cao, G., and Tian, J. (2018). Surface engineering of quantum dots for remarkably high detectivity photodetectors. *J. Phys. Chem. Lett.* *9*, 3285–3294.
- Tang, H., Zhong, J., Chen, W., Shi, K., Mei, G., Zhang, Y., Wen, Z., Müller-Buschbaum, P., Wu, D., Wang, K., and Sun, X.W. (2019). Lead sulfide quantum dot photodetector with enhanced responsivity through a two-step ligand-exchange method. *ACS Appl. Nano Mater.* *2*, 6135–6143.
- Tang, X., Ackerman, M.M., Chen, M., and Guyot-Sionnest, P. (2019). Dual-band infrared imaging using stacked colloidal quantum dot photodiodes. *Nat. Photonics* *13*, 277–282.

26. Lan, X., Voznyy, O., García de Arquer, F.P., Liu, M., Xu, J., Proppe, A.H., Walters, G., Fan, F., Tan, H., Liu, M., et al. (2016). 10.6% certified colloidal quantum dot solar cells via solvent-polarity-engineered halide passivation. *Nano Lett.* *16*, 4630–4634.
27. Kim, Y., Che, F., Jo, J.W., Choi, J., García de Arquer, F.P., Voznyy, O., Sun, B., Kim, J., Choi, M.J., Quintero-Bermudez, R., et al. (2019). A facet-specific quantum dot passivation strategy for colloid management and efficient infrared photovoltaics. *Adv. Mater.* *31*, e1805580.
28. Choi, H., Ko, J.H., Kim, Y.H., and Jeong, S. (2013). Steric-hindrance-driven shape transition in PbS quantum dots: understanding size-dependent stability. *J. Am. Chem. Soc.* *135*, 5278–5281.
29. Gilmore, R.H., Liu, Y., Shcherbakov-Wu, W., Dahod, N.S., Lee, E.M.Y., Weidman, M.C., Li, H., Jean, J., Bulović, V., Willard, A.P., et al. (2019). Epitaxial dimers and auger-assisted detrapping in PbS quantum dot solids. *Matter* *1*, 250–265.
30. Zhang, X., Zhang, J., Phuyal, D., Du, J., Tian, L., Öberg, V.A., Johansson, M.B., Cappel, U.B., Karis, O., Liu, J., et al. (2018). Inorganic CsPbI₃ perovskite coating on PbS quantum dot for highly efficient and stable infrared light converting solar cells. *Adv. Energy Mater.* *8*, 1702049.
31. Ning, Z., Gong, X., Comin, R., Walters, G., Fan, F., Voznyy, O., Yassitepe, E., Buin, A., Hoogland, S., and Sargent, E.H. (2015). Quantum-dot-in-perovskite solids. *Nature* *523*, 324–328.
32. Dirin, D.N., Dreyfuss, S., Bodnarchuk, M.I., Nedelcu, G., Papagiorgis, P., Itskos, G., and Kovalenko, M.V. (2014). Lead halide perovskites and other metal halide complexes as inorganic capping ligands for colloidal nanocrystals. *J. Am. Chem. Soc.* *136*, 6550–6553.
33. Gong, X., Yang, Z., Walters, G., Comin, R., Ning, Z., Beauregard, E., Adinolfi, V., Voznyy, O., and Sargent, E.H. (2016). Highly efficient quantum dot near-infrared light-emitting diodes. *Nat. Photonics* *10*, 253–257.
34. Noel, N.K., Habisreutinger, S.N., Wenger, B., Klug, M.T., Hörlantner, M.T., Johnston, M.B., Nicholas, R.J., Moore, D.T., and Snaith, H.J. (2017). A low viscosity, low boiling point, clean solvent system for the rapid crystallisation of highly specular perovskite films. *Energy Environ. Sci.* *10*, 145–152.
35. Quintero-Bermudez, R., Gold-Parker, A., Proppe, A.H., Munir, R., Yang, Z., Kelley, S.O., Amassian, A., Toney, M.F., and Sargent, E.H. (2018). Compositional and orientational control in metal halide perovskites of reduced dimensionality. *Nat. Mater.* *17*, 900–907.
36. Walravens, W., De Roo, J., Drijvers, E., ten Brinck, S., Solano, E., Dendooven, J., Detavernier, C., Infante, I., and Hens, Z. (2016). Chemically triggered formation of two-dimensional epitaxial quantum dot superlattices. *ACS Nano* *10*, 6861–6870.
37. Walters, G., Sutherland, B.R., Hoogland, S., Shi, D., Comin, R., Sellan, D.P., Bakr, O.M., and Sargent, E.H. (2015). Two-photon absorption in organometallic bromide perovskites. *ACS Nano* *9*, 9340–9346.
38. Nootz, G., Padilha, L.A., Olszak, P.D., Webster, S., Hagan, D.J., Van Stryland, E.W., Levina, L., Sukhovatkin, V., Brzozowski, L., and Sargent, E.H. (2010). Role of symmetry breaking on the optical transitions in lead-salt quantum dots. *Nano Lett.* *10*, 3577–3582.
39. Rossi, D., Wang, H., Dong, Y., Qiao, T., Qian, X., and Son, D.H. (2018). Light-induced activation of forbidden exciton transition in strongly confined perovskite quantum dots. *ACS Nano* *12*, 12436–12443.
40. Balazs, D.M., Rizkia, N., Fang, H.H., Dirin, D.N., Momand, J., Kooi, B.J., Kovalenko, M.V., and Loi, M.A. (2018). Colloidal quantum dot inks for single-step-fabricated field-effect transistors: the importance of postdeposition ligand removal. *ACS Appl. Mater. Interfaces* *10*, 5626–5632.
41. Sun, L., Choi, J.J., Stachnik, D., Bartnik, A.C., Hyun, B.R., Malliaras, G.G., Hanrath, T., and Wise, F.W. (2012). Bright infrared quantum-dot light-emitting diodes through inter-dot spacing control. *Nat. Nanotechnol.* *7*, 369–373.
42. Ip, A.H., Thon, S.M., Hoogland, S., Voznyy, O., Zhitomirsky, D., Debnath, R., Levina, L., Rollny, L.R., Carey, G.H., Fischer, A., et al. (2012). Hybrid passivated colloidal quantum dot solids. *Nat. Nanotechnol.* *7*, 577–582.
43. Proppe, A.H., Xu, J., Sabatini, R.P., Fan, J.Z., Sun, B., Hoogland, S., Kelley, S.O., Voznyy, O., and Sargent, E.H. (2018). Picosecond charge transfer and long carrier diffusion lengths in colloidal quantum dot solids. *Nano Lett.* *18*, 7052–7059.
44. Sanehira, E.M., Marshall, A.R., Christians, J.A., Harvey, S.P., Ciesielski, P.N., Wheeler, L.M., Schulz, P., Lin, L.Y., Beard, M.C., and Luther, J.M. (2017). Enhanced mobility CsPbI₃ quantum dot arrays for record-efficiency, high-voltage photovoltaic cells. *Sci. Adv.* *3*, eaao4204.
45. Ning, Z., Voznyy, O., Pan, J., Hoogland, S., Adinolfi, V., Xu, J., Li, M., Kirmani, A.R., Sun, J.P., Minor, J., et al. (2014). Air-stable n-type colloidal quantum dot solids. *Nat. Mater.* *13*, 822–828.